scientific reports

OPEN

Structural characterization of newly-developed Al$_{79}$Ni$_5$Fe$_5$Y$_{11}$ and Al$_{79}$Ni$_{11}$Fe$_5$Y$_5$ alloys with amorphous matrixes

Katarzyna Młynarek-Żak[1]✉, Indu Dhiman[2], Krzysztof Matus[3], Mariola Kądziołka-Gaweł[4], Wojciech Łoński[5], Adrian Radoń[6], Tomasz Czeppe[7] & Rafał Babilas[5]✉

The low glass-forming ability of aluminium-based metallic glasses significantly limits their development and preparation. This paper updates the current state of knowledge by presenting the results of structural studies of two newly-developed Al$_{79}$Ni$_5$Fe$_5$Y$_{11}$ and Al$_{79}$Ni$_{11}$Fe$_5$Y$_5$ alloys with a reduced aluminium content (< 80 at.%). The alloys were produced by conventional casting (ingots) and melt-spinning (ribbons). Structural characterization was carried out for bulk ingots first, and then for the melt-spun ribbons. The ingots possessed a multiphase crystalline structure, as confirmed by X-ray diffraction and scanning electron microscopy observations. The amorphous structure of the melt-spun ribbons was determined by X-ray diffraction and transmission electron microscopy. SEM observations and EDX element maps of the cross-section of melt-spun ribbons indicated a homogeneous elemental composition. Neutron diffraction revealed the presence of nanocrystals in the amorphous matrix of the melt-spun ribbons. DSC data of the melt-spun ribbons showed exothermic events corresponding to the first crystallization at temperatures of 408 °C and 387 °C for Al$_{79}$Ni$_5$Fe$_5$Y$_{11}$ and Al$_{79}$Ni$_{11}$Fe$_5$Y$_5$, respectively.

The first aluminium-based metallic glasses were developed in the late 1980s by Inoue et al.[1] and He et al.[2] The discovery of Al-based alloys with disordered amorphous structures aroused great interest among scientists due to reports of their high strength and corrosion resistance[2,3]. However, their low glass-forming ability (GFA) connected with the requirement for high critical cooling rates to avoid crystallization has significantly limited the practical applications of Al-based metallic glasses[4]. Melt-spinning, due to its ability to obtain high cooling rates, is the most commonly used foundry technology enabling the production of amorphous aluminium alloys[4]. Shen and Perepezko[4] explained that this is due to the low GFA of most Al-based alloy systems. In this method, a liquid metal is subjected to a very large cooling rate, which can reach 10^4–10^9 K/s. During the melt-spinning process, an ingot is placed in a ceramic crucible surrounded by an induction coil. Under the influence of alternating eddy currents, the temperature increases, which melts the charge material. The liquid metal is introduced onto a rapidly rotating copper wheel by a compressed gas[5,6].

According to ref.[4], the critical rate of cooling from the liquid state, which enables the glass transition of aluminium alloys, is 10^5–10^6 K/s. Therefore, these alloys are marginal glass formers or marginal metallic glasses. Despite their exceptional physical and chemical properties, the need to obtain them using high cooling rates limits the use of amorphous Al-based alloys to produce powders, wires, and ribbons. According to ref.[7], the key issue is the stabilization of the supercooled liquid, which can be achieved by shifting the time-temperature-transformation curve responsible for the beginning of crystallization to lower cooling rates by increasing the time. According to ref.[7], for this purpose, it is possible to minimize the amount of impurities in the alloy or to

[1]Department of Engineering Processes Automation and Integrated Manufacturing Systems, Silesian University of Technology, Konarskiego 18a St., 44-100 Gliwice, Poland. [2]Budapest Neutron Centre, Konkoly-Thege Miklos 29-33 St., Budapest 1121, Hungary. [3]Materials Research Laboratory, Faculty of Mechanical Engineering, Silesian University of Technology, Konarskiego 18a St, 44-100 Gliwice, Poland. [4]Institute of Physics, University of Silesia, 75 Pułku Piechoty 1 St., 41-500 Chorzów, Poland. [5]Department of Engineering Materials and Biomaterials, Silesian University of Technology, Konarskiego 18a St., 44-100 Gliwice, Poland. [6]Łukasiewicz Research Network, Institute of Non-Ferrous Metals, Sowinskiego 5 St., 44-100 Gliwice, Poland. [7]The Aleksander Krupkowski Institute of Metallurgy and Materials Science, Polish Academy of Sciences, Reymonta 25 St., 30-059 Kraków, Poland. ✉email: katarzyna.mlynarek-zak@polsl.pl; rafal.babilas@polsl.pl

develop methods for designing chemical compositions with a high GFA, taking into account thermodynamic and kinetic aspects.

Amorphous structure in Al-based alloys was determined for the alloy systems Al–Y–Fe[8], Al–Ni–Zr[9], Al–Fe–Zr[9], Al–Fe–Y[10,11], Al–Y–Ni[3], Al–Ni–Fe[12], Al–Ni–Y[13,14], Al–Ni–Fe–Gd[15], and Al–Ni–Y–Co–Fe[16]. The most popular Al-based metallic glasses are three-component alloys with transition metals (TMs) and rare-earth elements (REs)[8,17]. According to the assumptions described in ref.[8,18], the aluminium content should be in the range of 80–92 at.%, transition metals (TMs) 1–15 at.%, and rare earths (REs) 3–20%.

In this work, we present the results of structural studies of newly-developed $Al_{79}Ni_5Fe_5Y_{11}$ and $Al_{79}Ni_{11}Fe_5Y_5$ alloys. The aim of the article is to present new knowledge concerning Al-TMs-REs alloys with a reduced aluminium content produced by conventional casting and melt-spinning. The results presented in this paper will help facilitate the design of the chemical composition of Al-based metallic glasses. This paper contains the structural characteristics of slowly-cooled crystalline alloys in the form of ingots first and then rapidly-solidified amorphous ribbons cast by melt-spinning, as well as the results of differential scanning calorimetry.

Materials and methods

Two newly-developed $Al_{79}Ni_5Fe_5Y_{11}$ and $Al_{79}Ni_{11}Fe_5Y_5$ alloys with a reduced aluminium content (< 80 at.%) were studied. Ingots of Al, Ni, Fe, and Y elements with a purity of 99.99% were melted in an induction furnace under a protective argon atmosphere in cylindrical corundum crucibles and then slowly cooled. The dimensions of the ingots were 50 mm high and 30 mm in diameter. The ingots produced were remelted and cast into ribbons by rapidly cooling from the liquid state by melt-spinning using a Bühler Melt Spinner SC station. The linear speed of the copper wheel with a diameter of 200 mm via the melt-spinning method was 30 m/s, which corresponds to a rotational speed of approximately 2865 rpm. The ribbon casting temperature was 1400 °C for $Al_{79}Ni_5Fe_5Y_{11}$ alloy and 1200 °C for $Al_{79}Ni_{11}Fe_5Y_5$ alloy. The melt-spun ribbons were approximately 50 μm thick and 10 mm wide.

X-ray diffraction (XRD) patterns were recorded using a Mini Flex 600 equipped with a copper tube Cu Kα (λ = 0.154 nm) as the X-ray radiation source and a D/TEX strip detector. The XRD patterns were collected in the Bragg–Brentano geometry. Samples in the form of ribbons were powdered for XRD measurements.

Neutron diffraction studies of alloys in the form of melt-spun alloys were performed on the MTEST neutron powder diffractometer at the Budapest Neutron Center. The powdered ribbons were measured in vanadium cans with a diameter of 6 mm. The Cu (111) monochromator selected neutrons with a wavelength of λ = 0.145 nm.

Observations of the microstructures were made using a Cs-corrected transmission electron microscope S/TEM Titan 80–300 from FEI Company. High-resolution transmission electron microscopy (HRTEM) imaging was also used. The diffraction patterns were obtained with both selected area diffraction (SAED) and Fourier transformations from HRTEM images. The melt-spun samples in the form of circles with a diameter of 3 mm were processed by a precise ion polishing system (Gatan 691).

The microstructures of alloy ingots were characterized by scanning electron microscopy (EVO MA10, Carl Zeiss) using the backscattered electron (BSE) mode. The cross-sections of melt-spun ribbons were observed using the secondary electron (SE) mode (Supra 35, Carl Zeiss). The maps of chemical elements were obtained by using energy-dispersive X-ray spectroscopy (EDX).

^{57}Fe Mössbauer transmission spectra were recorded at room temperature with an MS96 Mössbauer spectrometer and a linearly-arranged ^{57}Co:Rh source. Numerical analysis of the Mössbauer spectra was performed using the WMOSS program.

The crystallization mechanisms of the studied alloys in the form of ribbons were described using differential scanning calorimetry (DSC). Two temperature ranges were used: from 200 to 1000 °C by using a thermal analyzer SDT Q600 (Al_2O_3/Al_2O_3) and from 200 to 700 °C by a 910 model (DuPont Company (Pt/Pt)).

Ethical approval

This article does not contain any studies with human participants or animals performed by any of the authors.

Results and discussion

To identify the structure of $Al_{79}Ni_5Fe_5Y_{11}$ and $Al_{79}Ni_{11}Fe_5Y_5$ alloys in the form of slowly-cooled ingots, X-ray diffraction was carried out. Figure 1 shows the XRD patterns with Miller indices for the identified phases. The studied ingots possessed a multiphase crystalline structure. The following phases were identified for the $Al_{79}Ni_5Fe_5Y_{11}$ alloy: $Al_{10}Fe_2Y$, Al_3Y, $Al_{23}Ni_6Y_4$, and α-Al. In the structure of the $Al_{79}Ni_{11}Fe_5Y_5$ alloy, three phases were identified: $Al_{19}Ni_5Y_3$, $Al_9Ni_{1.3}Fe_{0.7}$, and α-Al.

The X-ray phase analysis of the $Al_{85}Ni_5Fe_5Y_5$ alloy, with a similar chemical composition to the studied alloys, is presented in ref.[19]. Similarly to the studied alloys, this alloy contained α-Al. In addition, $Al_{23}Ni_6Y_4$ and $Al_{10}Fe_2Y$ phases were identified in the $Al_{79}Ni_5Fe_5Y_{11}$ alloy. In ref.[20], the authors proved that during annealing of the $Al_{86}Ni_8Y_6$ alloy with an amorphous structure, the $Al_{23}Ni_6Y_4$ phase crystallized first, followed by the α-Al phase due to the local depletion of nickel and yttrium in the metallic liquid. However, according to the research results described in ref.[21], the phase crystallization sequence in the alloy with a similar chemical composition $Al_{87}Ni_9Y_4$ is as follows: α-Al, Al_3Ni, and $Al_{19}Ni_5Y_3$. The $Al_{23}Ni_6Y_4$ phase was identified in the $Al_{79}Ni_5Fe_5Y_{11}$ alloy, while the presence of the $Al_{19}Ni_5Y_3$ phase was demonstrated for the $Al_{79}Ni_{11}Fe_5Y_5$ alloy. Similarly to ref.[20], the Al_3Ni phase was not identified, which should be present, according to the Al–Ni–Y phase equilibrium diagram. On the other hand, the Al_3Y phase was identified only for the $Al_{79}Ni_5Fe_5Y_{11}$ alloy, which resulted from the higher atomic content of yttrium. Al–Fe phases were not found in the $Al_{79}Ni_{11}Fe_5Y_5$ alloy, probably due to the depletion of iron in the alloy after crystallization of the $Al_9Ni_{1.3}Fe_{0.7}$ and $Al_{10}Fe_2Y$ phases.

The presence of a multiphase crystalline structure in the $Al_{79}Ni_5Fe_5Y_{11}$ and $Al_{79}Ni_{11}Fe_5Y_5$ ingots was confirmed by microstructure observations using SEM. The images of the microstructures in the backscattered electron (BSE)
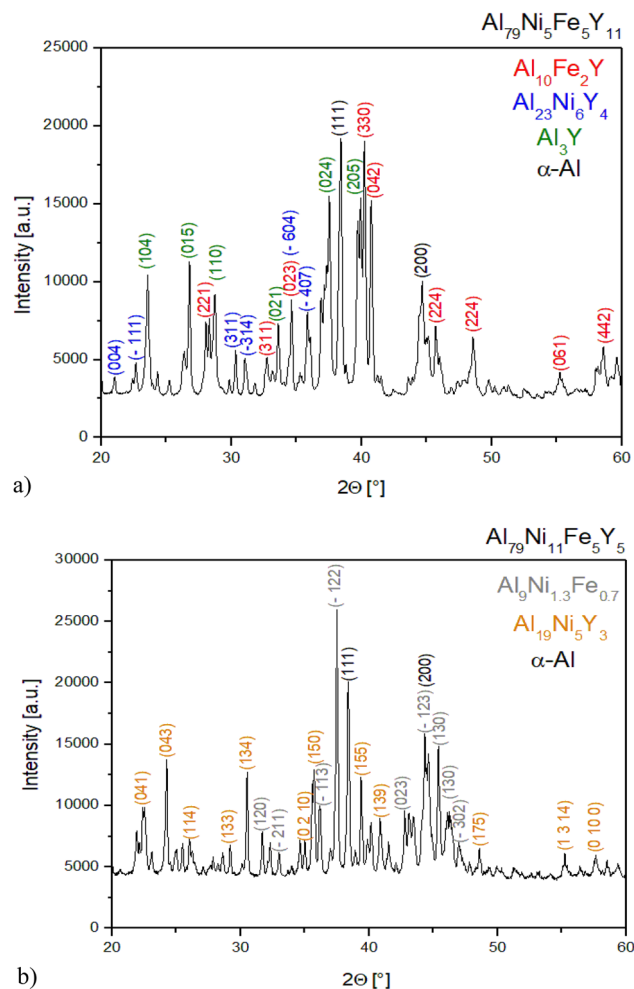
Figure 1. X-ray diffraction patterns of $Al_{79}Ni_5Fe_5Y_{11}$ (**a**) and $Al_{79}Ni_{11}Fe_5Y_5$ (**b**) in the form of ingots.

mode and the EDX element distribution maps are shown in Fig. 2. In the studied alloys, phases consisting of aluminium, nickel, and yttrium ($Al_{19}Ni_5Y_3$ and $Al_{23}Ni_6Y_4$) were present in the form of lamellar precipitates. The EDX maps confirmed the presence of the α-Al phase due to the presence of areas characteristic of aluminium (marked in red). This was confirmed by the presence of the α-Al phase, for which two high-intensity peaks were identified in the XRD patterns in studied ingots.

The microstructures of Al–Zr–Ni–Fe–Y alloys in the form of ingots are presented in ref.[22], in which the Al_3Y phase was present in the form of small platelets. However, the Al_3Y phase in the SEM microstructures of Al-Y-Fe master alloys was observed in the form of longitudinal, regular precipitates in ref.[23]. The $Al_{10}Fe_2Y$ phase in the $Al_{88}Y_{8-x}Fe_{4+x}$ alloys ($x = 0, 1, 2$ at. %) formed a dendritic structure, while the α-Al phase was the matrix, which was characterized by the darkest shade in the SEM images in the studied alloys[23]. Xu et al.[24] presented the microstructure of an Al–Ni–Y alloy produced using slow cooling and under pressure. Using both solidification methods, the $Al_{88}Ni_7Y_5$ alloy consisted of α-Al, $Al_3(Ni,Y)$ and $Al(Ni,Y)$ phases. The slowly cooled alloy was characterized by a structure consisting of thick plates of the $Al_3(Ni,Y)$ phase and thin needles of the $Al(Ni,Y)$ phase. Cooling under a pressure of 6 GPa changed the coarse-grained $Al_3(Ni,Y)$ phase into branched dendrites[24]. The presence of thick, lamellar precipitates of the Al–Ni–Y phases was also observed in the studied alloys. Similar microstructures were also presented in ref.[25] for the multiphase $Al_{85}Ni_7Fe_4La_4$ alloy in the form of an ingot. The α-Al phase, similar to the studied alloys, was identified as the darkest precipitates. In ref.[25], the authors indicated the phase marked $Al_9Ni_{1-x}Fe_x$ as oblong, oriented along one direction of the plate. In the case of the studied alloys, the largest number of reflections for the $Al_9Ni_{1.3}Fe_{0.7}$ phase was identified in the XRD patterns of the $Al_{79}Ni_{11}Fe_5Y_5$ alloy. Based on the EDX maps, the $Al_9Ni_{1.3}Fe_{0.7}$ phase was marked in the SEM image as medium-gray precipitates. In contrast to the microstructure described in ref.[25], an orientation along one direction was not observed for the $Al_9Ni_{1.3}Fe_{0.7}$ phase.

Figure 3 presents the XRD patterns of melt-spun $Al_{79}Ni_5Fe_5Y_{11}$ and $Al_{79}Ni_{11}Fe_5Y_5$ alloys, which indicates an amorphous structure because of the characteristic amorphous "halo" and the lack of crystalline reflections. However, the XRD pattern of $Al_{79}Ni_{11}Fe_5Y_5$ was characterized by a broad peak that indicated a double-amorphous state.

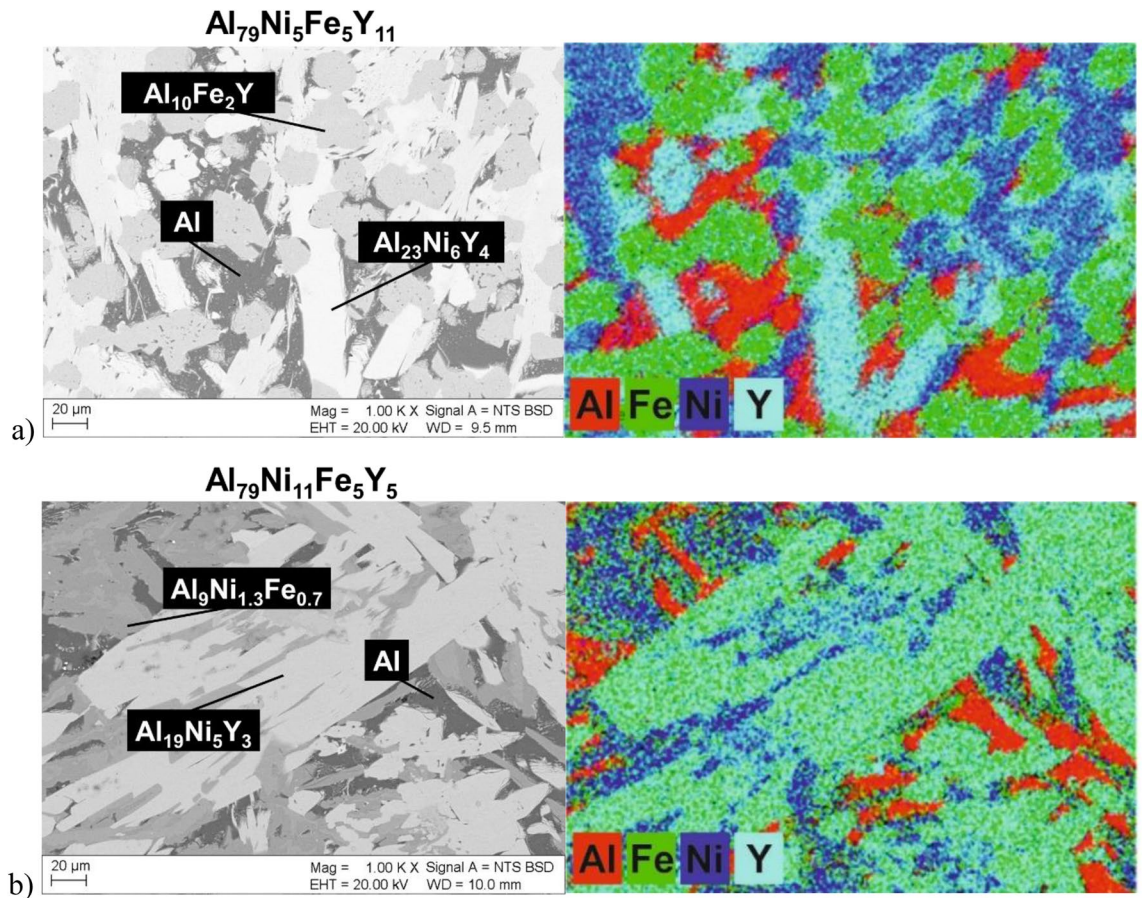**Figure 2.** SEM images of the microstructures of $Al_{79}Ni_5Fe_5Y_{11}$ (**a**) and $Al_{79}Ni_{11}Fe_5Y_5$ (**b**) alloys in the form of ingots in BSE mode with element distribution maps.
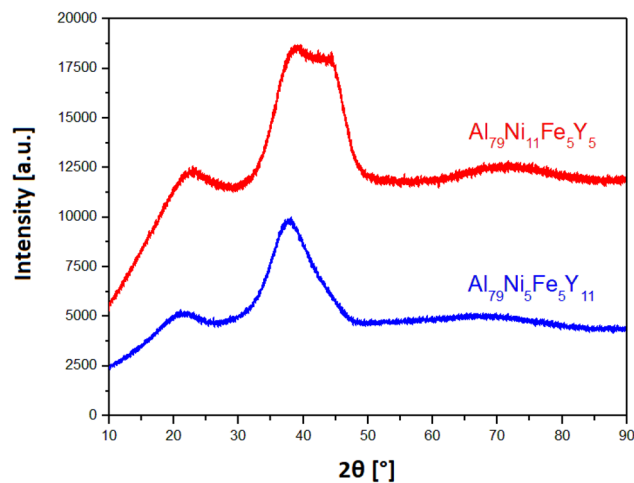
Figure 3. X-ray diffraction patterns of $Al_{79}Ni_{11}Fe_5Y_5$ and $Al_{79}Ni_5Fe_5Y_{11}$ in the form of ribbons.

According to ref.[20], the $Al_{23}Ni_6Y_4$ phase limits the vitrification of Al–Ni–Y alloys because it was identified as the primary phase during the crystallization of the amorphous $Al_{86}Ni_8Y_6$ alloy. However, in the case of the $Al_{79}Ni_5Fe_5Y_{11}$ alloy in the form of an ingot, the $Al_{23}Ni_6Y_4$ phase was identified. An amorphous structure was obtained for the ribbons with this chemical composition. According to previous literature[8,17], Al-TM-RE alloys with a disordered atomic structure should contain 80–92 at.% aluminium. Despite the reduced content of the main alloying element, an amorphous structure was obtained for the $Al_{79}Ni_{11}Fe_5Y_5$ and $Al_{79}Ni_5Fe_5Y_{11}$ alloys.

To confirm the amorphous structure of $Al_{79}Ni_5Fe_5Y_{11}$ and $Al_{79}Ni_{11}Fe_5Y_5$ alloys in the form of melt-spun ribbons, TEM observations were carried out. Figure 4 shows the HRTEM images and selected area electron diffractions (SAED) pattern. The microscopic observations showed that the studied alloys were characterized by a homogeneous structure devoid of crystallites. Structures in the high-resolution mode were characterized by atomic disorder, referred to in the literature[26] as the "salt and pepper" effect. In addition, the presence of an amorphous structure for the $Al_{79}Ni_5Fe_5Y_{11}$ and $Al_{79}Ni_{11}Fe_5Y_5$ alloys was confirmed by the SAED results due to the broadened ring patterns.

The elemental distributions were collected for $Al_{79}Ni_5Fe_5Y_{11}$ (Fig. 5) and $Al_{79}Ni_{11}Fe_5Y_5$ (Fig. 6) alloys in ribbon form. The external morphology of the samples was also obtained in SE mode. The alloys were assigned as homogeneous single-phase structures with no segregation. It can be seen that the maps presented areas with different concentrations of Al, Ni, Fe, and Y elements according to the nominal chemical compositions of the samples. The homogeneous concentration of the elements also confirmed the amorphous structure of the tested ribbons. Previous works[27,28] have reported that an amorphous structure was obtained on the surface as a result of contact with the copper wheel during the melt-spinning process. The influence of material surface contact during cooling on the structure was described, i.e., for Ti–Ni–Cu alloys produced by the melt-spinning method.
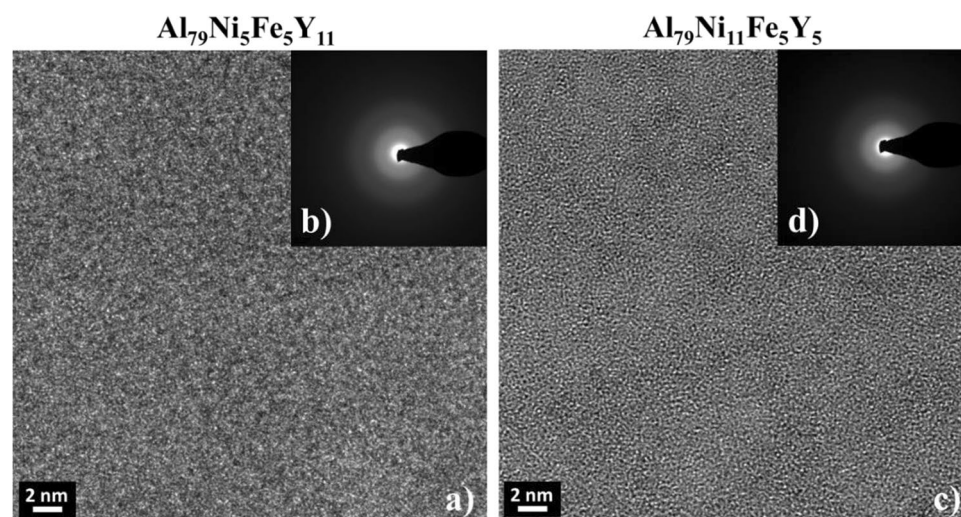

Figure 4. HRTEM images (**a**, **c**) and SAED patterns (**b**, **d**) of the $Al_{79}Ni_5Fe_5Y_{11}$ and $Al_{79}Ni_{11}Fe_5Y_5$ alloys in the form of melt-spun ribbons.

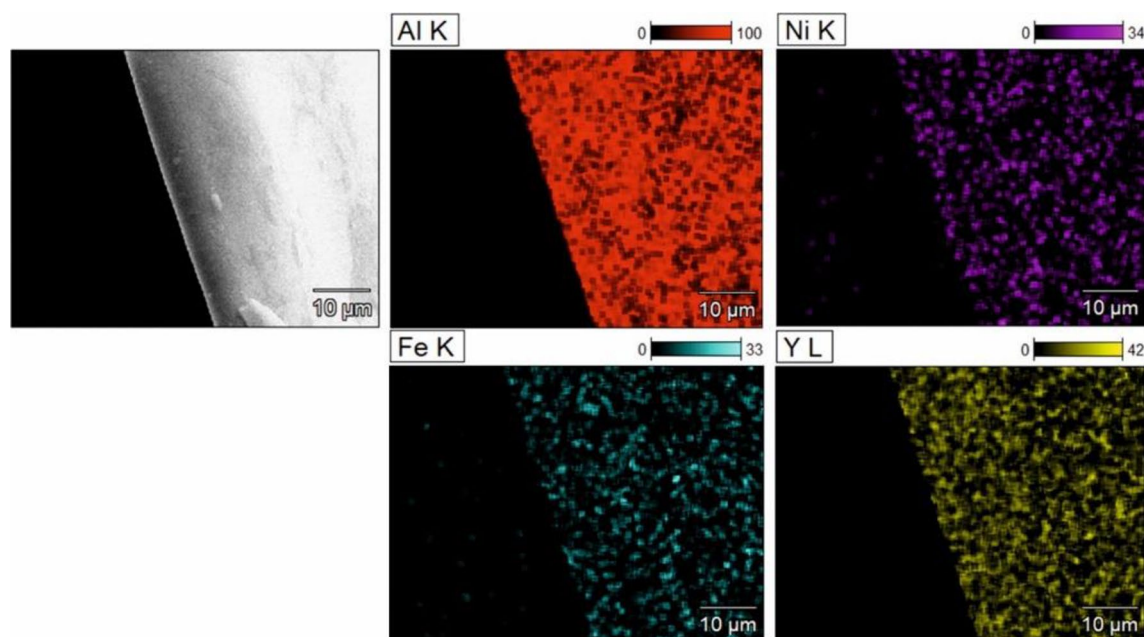**Figure 5.** Microstructure of $Al_{79}Ni_5Fe_5Y_{11}$ alloy in ribbon form with EDX element distribution maps.

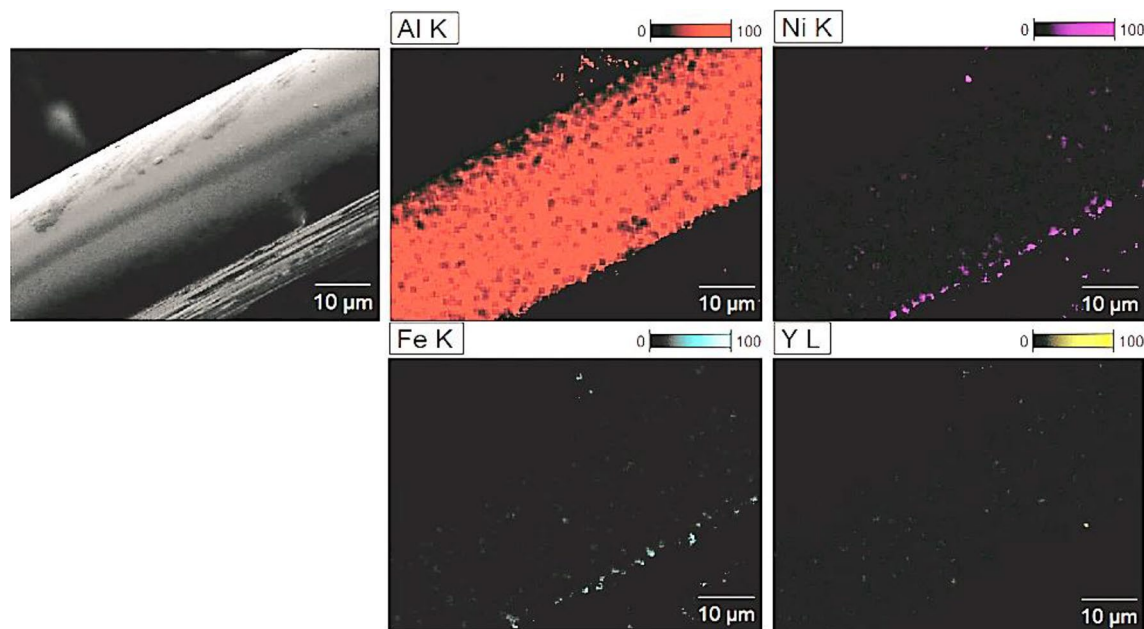**Figure 6.** Microstructure of $Al_{79}Ni_{11}Fe_5Y_5$ alloy in ribbon form with EDX element distribution maps.

An amorphous zone (called the contact surface) and the crystalline zone (called the free surface) were visible on the cross-sectional SEM images of the studied ribbons[27].

Figure 7 shows the neutron diffraction patterns of the alloys in the form of melt-spun ribbons. Broad diffraction peaks indicating the reflections of crystallites were observed for both alloys. The reflections for the α-Al and Al_8Fe_4Y phases were identified for the $Al_{79}Ni_5Fe_5Y_{11}$ alloy, while reflections for the Al_8Fe_4Y phase were observed for the $Al_{79}Ni_{11}Fe_5Y_5$ alloy. The penetration depth of neutrons in matter is much deeper compared with X-rays and electrons; therefore, according to ref.[29], neutron radiation is useful for studying bulk materials. According to literature data[30,31], the amorphous structure of metallic glasses should make them resistant to irradiation. Yang et al.[30] studied the structural responses of ZrCu metallic glasses under neutron irradiation and did not observe the formation of any crystalline phase, even though they confirmed its presence by synchrotron-based high-energy X-ray diffraction. However, in the same article[30], the mechanisms of neutron irradiation that damaged the microstructure of amorphous alloys remained elusive. In this study, the melt-spun ribbons likely had a heterogeneous structure.

Mössbauer spectra with their adjustments obtained for the $Al_{79}Ni_5Fe_5Y_{11}$ and $Al_{79}Ni_{11}Fe_5Y_5$ alloys in the form of ribbons are shown in Fig. 8. These spectra were fitted with non-magnetic components (quadrupole doublets)[32]. The determined hyperfine parameters of these components are summarized in Table 1. The spectrum of the $Al_{79}Ni_{11}Fe_5Y_5$ alloy contained two doublets, indicating the presence of two different local environments of iron atoms. The isomeric shifts (Is) of both these doublets were similar and in the range of 0.19–0.21 mm/s, but these components differed significantly in their quadrupole splitting (Qs). The Qs range was 0.25–0.29 mm/s for the first doublet, and 0.54–0.56 mm/s for the second. Taking into account the XRD results for these alloys, we can
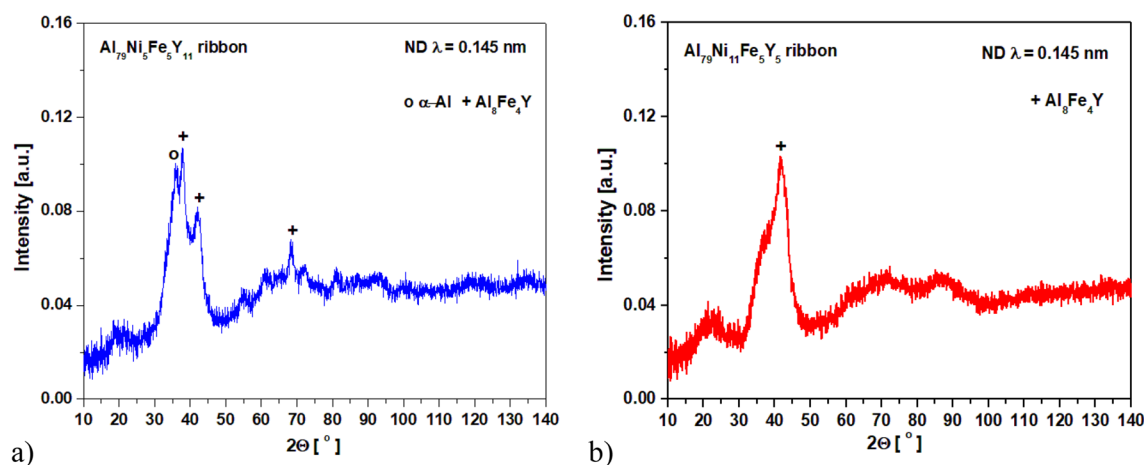

Figure 7. Neutron diffraction patterns of $Al_{79}Ni_5Fe_5Y_{11}$ (**a**) and $Al_{79}Ni_{11}Fe_5Y_5$ (**b**) alloys in the form of ribbons.
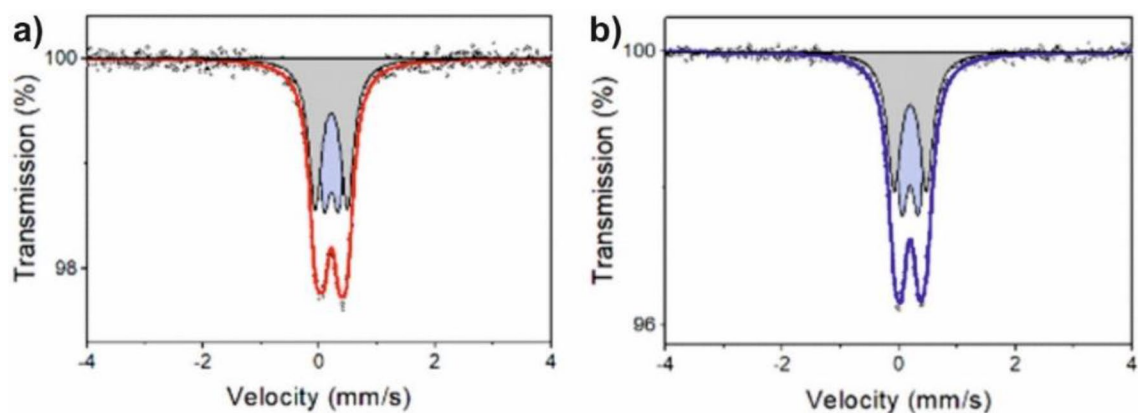
Figure 8. Mössbauer spectra of $Al_{79}Ni_5Fe_5Y_{11}$ (**a**) and $Al_{79}Ni_{11}Fe_5Y_5$ alloys (**b**).

Alloy	Is (mm/s)	Qs (mm/s)	FWHM (mm/s)	A (%)	Phase
$Al_{79}Ni_5Fe_5Y_{11}$	0.21	0.25	0.27	47	Rich in Al, Fe, Y
	0.21	0.55		53	Rich in Al, Fe, Ni
	0.21*	0.42*	0.26	–	–
$Al_{79}Ni_{11}Fe_5Y_5$	0.19	0.28	0.28	51	Rich in Al, Fe, Y
	0.20	0.56		49	Rich in Al, Fe, Ni
	0.20*	0.41*	0.26*	–	–

Table 1. The Mössbauer hyperfine parameters of the investigated samples. *Is* - isomer shift, *Qs* - quadrupole splitting, *FWHM* - full width at half maximum, *A* - relative area from the spectra, * - parameters related to p(Qs) of $Al_{79}Ni_5Fe_5Y_{11}$ and $Al_{79}Ni_{11}Fe_5Y_5$ alloys in the form of ribbons.

associate these doublets with the presence of iron in the aluminium-rich amorphous structure[33]. The diffraction pattern of the $Al_{79}Ni_5Fe_5Y_{11}$ alloy in the form of ribbons indicated the presence of an amorphous structure, while that of the $Al_{79}Ni_{11}Fe_5Y_5$ alloy was characterized by a double "halo," indicating the presence of two types of atomic disorder. The significantly different quadrupole splitting values of these two doublets resulted from different local geometries of the distributions of nickel and yttrium atoms around iron atoms[23]. The component with higher values of quadrupole splitting will be associated with iron atoms having mainly aluminium and yttrium in their local environments, and the doublet with lower *Qs* values will be associated with iron atoms surrounded mainly by aluminium and nickel atoms. Yttrium atoms with a larger atomic radius than nickel atoms caused greater distortion of the local iron environment, hence higher values of quadrupole splitting.

To describe the thermal events under heating and cooling, the crystalline alloys (in the form of ingots) and amorphous ribbons were analyzed using DSC. As seen in Fig. 9, the DSC curve of the $Al_{79}Ni_5Fe_5Y_{11}$ ingot showed three endothermic peaks at 637 °C, 890 °C and 982 °C during heating from room temperature to 1100 °C,
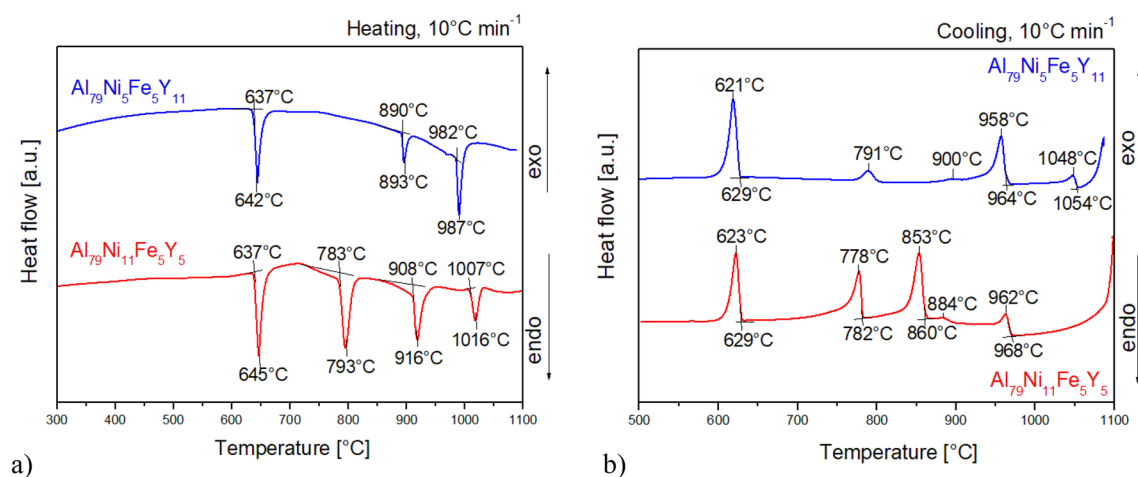

Figure 9. DSC heating (**a**) and cooling (**b**) curves of $Al_{79}Ni_5Fe_5Y_{11}$ and $Al_{79}Ni_{11}Fe_5Y_5$ alloys in the form of ingots.

indicating the occurrence of phase transformations. On the other hand, during cooling from 1100 °C to room temperature, five exothermic peaks were observed at 1048 °C, 958 °C, 900 °C, 791 °C and 621 °C. The DSC curve of the $Al_{79}Ni_{11}Fe_5Y_5$ ingot showed four endothermic peaks at 637 °C, 783 °C, 908 °C and 1007 °C, while during cooling, five exothermic peaks were observed at 962 °C, 884 °C, 853 °C, 778 °C and 623 °C. According to literature data[19,22,34], the thermal event above 600 °C probably corresponded to the melting of the α-Al phase during heating and its crystallization during cooling.

Figure 10 shows the DSC curves recorded in the temperature range of 200–1000 °C at the rate of 10 °C/min during heating for $Al_{79}Ni_5Fe_5Y_{11}$ and $Al_{79}Ni_{11}Fe_5Y_5$ alloys in the form of ribbons. Figure 11 also shows the DSC curves for the same ribbons over a smaller temperature range (200–700 °C) and with a higher heating rate (20 °C/min). In the DSC curves (Fig. 10), three exothermic events appeared during heating at 390 °C, 433 °C, and 499 °C for $Al_{79}Ni_{11}Fe_5Y_5$ ribbon. Moreover, three endothermic events at 630 °C, 796 °C and 922 °C were also recorded. The DSC curve of the $Al_{79}Ni_5Fe_5Y_{11}$ ribbon showed one clear exothermic peak recorded at 412 °C as well as endothermic event at 630 °C. An endothermic reaction with a low enthalpy was also recorded at 900 °C. The recorded baseline for the ribbon with a higher yttrium content was characterized by an unstable course, probably related to the movement of metallic liquid in the measuring crucible. Based on the DSC curves shown in Fig. 11, T_x (onset crystallization temperature), T_p (crystallization peak temperature), and T_m (melting temperature) were determined. The $Al_{79}Ni_{11}Fe_5Y_5$ alloy was characterized by a lower temperature at the beginning of crystallization of the amorphous phase (T_x = 390 °C) compared with $Al_{79}Ni_5Fe_5Y_{11}$ alloy (T_x = 408 °C). Similarly to Fig. 10, two additional exothermic events were observed for the $Al_{79}Ni_{11}Fe_5Y_5$ alloy with crystallization temperatures of 434 °C and 507 °C. The $Al_{79}Ni_{11}Fe_5Y_5$ (T_m = 632 °C) and $Al_{79}Ni_5Fe_5Y_{11}$ (T_m = 631 °C) alloys were characterized by similar melting onset temperatures determined from the recorded endothermic event.

A similar course of the DSC curve as the $Al_{79}Ni_{11}Fe_5Y_5$ ribbons was presented in ref.[35] for the $Al_{84.5}Ni_{5.5}Y_{10}$ alloy with an amorphous structure in the form of a high-pressure cast rod. In ref.[35], three distinct, consecutive exothermic events and one endothermic event were recorded. Fu et al.[35] stated that the exothermic peaks
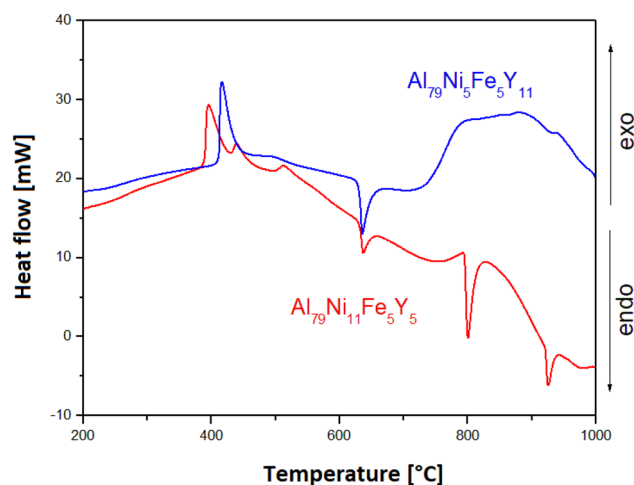

Figure 10. DSC heating curves of $Al_{79}Ni_5Fe_5Y_{11}$ and $Al_{79}Ni_{11}Fe_5Y_5$ alloys in the form of melt-spun ribbons.
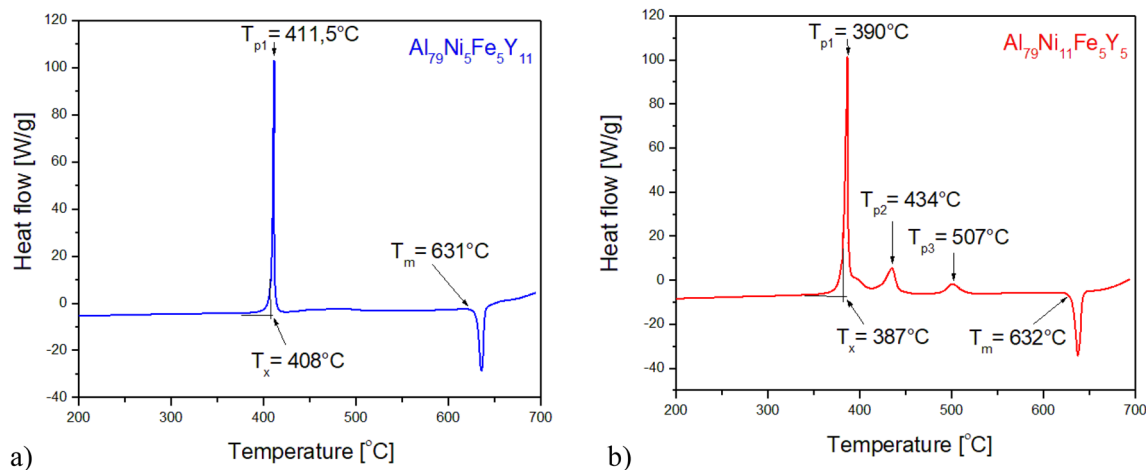
Figure 11. DSC heating curves of $Al_{79}Ni_5Fe_5Y_{11}$ (**a**) and $Al_{79}Ni_{11}Fe_5Y_5$ (**b**) alloys in the form of melt-spun ribbons.

corresponded to the crystallization of the amorphous structure, while the endothermic event was related to the glass transition. However, on the basis of ref.[4,36] most of Al-based metallic glasses do not show a clear T_g glass-transition event because the onset of the T_x primary crystallization peak almost coincides with the glass transition. Moreover, according to the authors of ref.[35], the liquid phase was present in practically the entire volume of the alloy after the first endothermic peak. On the basis of the DSC curve in ref.[35], the glass transition temperature (T_g), onset crystallization temperature (T_{x1}), melting point (T_m), and liquidus temperature (T_l) were determined, respectively, as 207 °C, 244 °C, 617 °C, and 959 °C. Exothermic effects recorded for the $Al_{79}Ni_{11}Fe_5Y_5$ alloy occurred at higher temperatures due to differences in the chemical composition of the amorphous phase. In addition, two additional endothermic effects were observed in the DSC curve for the $Al_{79}Ni_{11}Fe_5Y_5$ alloy. The crystallization mechanisms of $Al_{85}Ni_{10}Y_5$ and $Al_{85}Ni_5Fe_5Y_5$ alloys are described in ref.[34] based on the XRD patterns obtained in situ at variable temperatures and the results of differential thermal analysis (DTA). Similarly to the $Al_{79}Ni_5Fe_5Y_{11}$ and $Al_{79}Ni_{11}Fe_5Y_5$ alloys, exothermic effects related to the crystallization of the amorphous phase were recorded on the DTA curves. On the basis of the diffractograms, it was estimated that in the $Al_{85}Ni_{10}Y_5$ alloy, after the formation of the α-Al phase, the $Al_{19}Ni_5Y_3$ phase crystallized at 340 °C. The temperature of 400 °C was associated with the crystallization of the $Al_{15}Fe_9Y_2$ phase in both the $Al_{85}Ni_{10}Y_5$ and $Al_{85}Ni_5Fe_5Y_5$ alloys. According to ref.[34], the last stage was the crystallization of the AlNiY and $Fe_{0.7}Ni_{1.3}Al_9$ phases.

Conclusions

The ingots possessed a multiphase crystalline structures. Melt-spinning method was used to obtain supercooled alloys in the form of ribbons. The amorphous structure of the ribbons was confirmed by XRD, SEM, and TEM, however the results of neutron diffraction studies indicate that the melt-spun alloys exhibited amorphous matrix structure with the presence of crystalline phases. The diffraction pattern of the $Al_{79}Ni_5Fe_5Y_{11}$ ribbon indicated the presence of an amorphous structure, while the $Al_{79}Ni_{11}Fe_5Y_5$ alloy was characterized by a double-broadened peak that indicated the presence of two types of atomic disorder. Furthermore, exothermic events in the DSC curves indicated the occurrence of crystallization from the amorphous phase at 408 °C for the $Al_{79}Ni_5Fe_5Y_{11}$ alloy and at 387 °C for the $Al_{79}Ni_{11}Fe_5Y_5$ alloy.

Data availability

The data and material generated during and/or analyzed during the current study are available from the corresponding author upon reasonable request.

References

1. Inoue, A., Ohtera, K., Tsai, A. P. & Masumoto, T. Aluminum-based amorphous alloys with tensile strength above 980 MPa (100 kg/mm²). *Jpn. Soc. Appl. Phys.* **27**, L479–L482 (1988).
2. He, Y., Poon, S. J. & Shiflet, G. J. Synthesis and properties of metallic glasses that contain aluminum. *Science* **241**, 1640–1642 (1988).
3. Kim, Y. H., Inoue, A. & Masumoto, T. Increase in mechanical strength of Al–Y–Ni amorphous alloys by dispersion of nanoscale fcc-Al particles. *Mater. Trans. JIM* **32**, 331–338 (1991).
4. Shen, Y. & Perepezko, J. H. Al-based amorphous alloys: Glass-forming ability, crystallization behavior and effects of minor alloying additions. *J. Alloys Compd.* **707**, 3–11 (2017).
5. Suryanarayana, C. & Inoue, A. *Bulk Metallic Glasses* (CRC Press, 2011).
6. El-Eskandarany, M. S. Introduction. in *Mechanical Alloying For Fabrication of Advanced Engineering Materials* 1–12 (William Andrew Inc., 2015).
7. Zhang, C., Ouyang, D., Pauly, S. & Liu, L. 3D printing of bulk metallic glasses. *Mater. Sci. Eng. R Rep.* **145**, 100625 (2021).
8. Saksl, K., Jóvári, P., Franz, H. & Jiang, J. Z. Atomic structure of Al₈₈Y₇Fe₅ metallic glass. *J. Appl. Phys.* **97**, 1–8 (2005).
9. Blank-Bewersdorff, M. Crystallization behaviour of Al₈₆Ni₁₀Zr₄ and Al₈₆Fe₁₀Zr₄ metallic glasses. *J. Mater. Sci. Lett.* **10**, 1225–1227 (1991).
10. Li, Q., Johnson, E., Madsen, M. B., Johansen, A. & Sarholt-Kristensen, L. Crystallization of Al-based metallic glasses structural aspects. *Philos. Mag. B Phys. Condens. Matter; Stat Mech. Electron. Opt. Magn. Prop.* **66**, 427–442 (1992).
11. Gao, M. C., Hackenberg, R. E. & Shiflet, G. J. Deformation-induced nanocrystal precipitation in Al-base metallic glasses. *Mater. Trans.* **42**, 1741–1747 (2001).
12. Inoue, A., Horio, Y. & Masumoto, T. New amorphous Al–Ni–Fe and Al–Ni–Co alloys. *Mater. Trans. JIM* **34**, 85–88 (1993).
13. Jiang, X. Y., Zhong, Z. C. & Greer, A. L. Particle-size effects in primary crystallization of amorphous Al–Ni–Y alloys. *Mater. Sci. Eng. A* **226–228**, 789–793 (1997).
14. He, Y., Shiflet, G. J. & Poon, S. J. Synthesis and properties of aluminum-based metallic glasses containing rare earths. *J. Alloys Compd.* **207–208**, 349–354 (1994).
15. He, Y., Dougherty, G. M., Shiflet, G. J. & Poon, S. J. Unique metallic glass formability and ultra-high tensile strength in Al–Ni–Fe–Gd alloys. *Acta Metall. Mater.* **41**, 337–343 (1993).
16. Yan, M., Wang, J. Q., Kong, C., Schaffer, G. B. & Qian, M. Micrometer-sized quasicrystals in the Al₈₅Ni₅Y₆Co₂Fe₂ metallic glass: A TEM study and a brief discussion on the formability of quasicrystals in bulk and marginal glass-forming alloys. *J. Mater. Res.* **27**, 2131–2139 (2012).
17. Inoue, A. Amorphous, nanoquasicrystalline and nanocrystalline alloys in Al-based systems. *Prog. Mater. Sci.* **43**, 365–520 (1998).
18. Fan, C. *et al.* Recent topics on the structure and crystallization of Al-based glassy alloys. *Mater. Res.* **22**, 1–15 (2019).
19. Babilas, R. *et al.* Influence of Fe, Cr, and Cu addition on the microstructure, hardness, and anticorrosion properties of Al–Ni–Y alloys. *Arch. Civ. Mech. Eng.* **22**, 1–15 (2022).
20. Kuball, A., Stolpe, M. & Busch, R. Crystallization behavior of the Al₈₆Ni₈Y₆ metallic glass forming alloy upon rapid cooling. *J. Alloys Compd.* **737**, 398–404 (2018).
21. Styles, M. J. *et al.* On the competition in phase formation during the crystallisation of Al–Ni–Y metallic glasses. *Acta Mater.* **117**, 170–187 (2016).
22. Babilas, R., Łoński, W., Młynarek, K., Bajorek, A. & Radoń, A. Relationship between the thermodynamic parameters, structure, and anticorrosion properties of Al–Zr–Ni–Fe–Y alloys. *Metall. Mater. Trans. A Phys. Metall. Mater. Sci.* **51**, 4215–4227 (2020).

23. Babilas, R. *et al.* Glass-forming ability and corrosion resistance of $Al_{88}Y_{8-x}Fe_{4+x}$ (x= 0, 1, 2 at.%) alloys. *Materials (Basel)* **14**, 1–12 (2021).
24. Xu, R. The effect of high pressure on solidification microstructure of Al–Ni–Y alloy. *Mater. Lett.* **59**, 2818–2820 (2005).
25. Vasiliev, A. L. *et al.* Microstructural peculiarities of Al-rich Al–La–Ni–Fe alloys. *Metall. Mater. Trans. A Phys. Metall. Mater. Sci.* **50**, 1995–2013 (2019).
26. Song, Y. *et al.* Crystallization of cobalt amorphous alloys under field annealing. *J. Nanosci. Nanotechnol.* **12**, 1074–1083 (2012).
27. Shelyakov, A. V. *et al.* Fabrication and characterization of amorphous-crystalline TiNiCu melt-spun ribbons. *J. Alloys Compd.* **577**, 251–254 (2013).
28. Shelyakov, A. *et al.* Design of microgrippers based on amorphous-crystalline TiNiCu alloy with two-way shape memory. *J. Micro-Bio Robot.* **16**, 43–51 (2020).
29. Barandiarán, J. M. *et al.* Neutron and synchrotron studies of structure and magnetism of Shape Memory Alloys. *J. Phys. Conf. Ser.* **663**, 1–9 (2015).
30. Yang, L. *et al.* Structural responses of metallic glasses under neutron irradiation. *Sci. Rep.* **7**, 1–13 (2017).
31. Mayr, S. G. Impact of ion irradiation on the thermal, structural, and mechanical properties of metallic glasses. *Phys. Rev. B - Condens. Matter Mater. Phys.* **71**, 1–7 (2005).
32. Dunlap, R. A., Dahn, J. R., Eelman, D. A. & MacKay, G. R. Microstructure of supersaturated fcc Al–Fe alloys: A comparison of rapidly quenched and mechanically alloyed $Al_{98}Fe_2$. *Hyperfine Interact.* **116**, 117–126 (1998).
33. Babilas, R. *et al.* Analysis of thermodynamic parameters for designing quasicrystalline Al–Ni–Fe alloys with enhanced corrosion resistance. *J. Alloys Compd.* **868**, 1–11 (2021).
34. Babilas, R. *et al.* Study of crystallization mechanism of Al-based amorphous alloys by in-situ high temperature X-ray diffraction method. *Sci. Rep.* **12**, 1–8 (2022).
35. Fu, H. M. *et al.* Synthesis and compressive properties of Al–Ni–Y metallic glass. *Philos. Mag. Lett.* **89**, 711–716 (2009).
36. Wu, R. I., Wilde, G. & Perepezko, J. H. Glass formation and primary nanocrystallization in Al-base metallic glasses. *Mater. Sci. Eng. A* **301**, 12–17 (2001).

Author contributions

K.M-Ż. and R.B. developed the methodology and assumptions of the experiments. I.D. conducted research using neutron diffraction. K.M. conducted and interpreted the structural analysis using transmission electron microscopy. A.R. conducted XRD studies. M.K-G. conducted Mössbauer spectroscopy studies. M.K-G. and K.M-Ż. interpreted Mössbauer spectroscopy results. K.M-Ż. and W.Ł. conducted SEM observations. T.C. and K.M-Ż. carried out and interpreted DSC measurements. K.M-Ż. wrote the main manuscript text. R.B. was responsible for supervision over research works and results analysis of experiments, reviewing and editing. All authors reviewed and approved the manuscript.

Funding

Competing interests

The authors declare no competing interests.

Additional information

Correspondence and requests for materials should be addressed to K.M. or R.B.

Reprints and permissions information is available at www.nature.com/reprints.

Publisher's note Springer Nature remains neutral with regard to jurisdictional claims in published maps and institutional affiliations.